



Full length article

# The role of solute clusters in the nucleation of precipitates in Al–Mg–Si–Cu alloys

J.R. Famelton <sup>a</sup>,\* C.A. Williams <sup>b</sup>, C. Barbatti <sup>c</sup>, P.A.J. Bagot <sup>d</sup>, M.P. Moody <sup>d</sup>

<sup>a</sup> Brunel Centre for Advanced Solidification Technology, Brunel University, London, UK

<sup>b</sup> Innoval Technology Ltd, Rotherham, UK

<sup>c</sup> Constellium University Technology Centre, Brunel University, London, UK

<sup>d</sup> Department of Materials, University of Oxford, Oxford, UK

## ARTICLE INFO

### Keywords:

Cluster assisted nucleation  
Atom probe tomography  
Al alloys  
Ageing  
Al–Mg–Si–Cu

## ABSTRACT

In this work the precipitation behaviour of both high and low Cu variants of a Al-6xxx alloy were investigated with and without natural ageing. The material yield strength was greater in the high Cu alloy and without natural ageing. The strength was seen to correspond to changes in precipitate number density and a mechanism of dislocation bowing around these precipitates. In the samples without natural ageing, Cu was seen to increase the number density of nuclei and hence the final precipitate number density. In the samples with natural ageing, solute clusters were observed to dissolve during subsequent artificial ageing, but a higher proportion remained in the high Cu alloy and acted as nucleation sites for further precipitation.

## 1. Introduction

The negative effect of natural ageing on 6xxx series alloys is well established and it is thought that the solute clusters formed during natural ageing lead to this effect [1,2]. The precipitation sequence of these alloys is often given as;

$$SSSS \rightarrow \text{solute clusters} \rightarrow GP \text{ zones} \rightarrow pre - \beta'' \rightarrow \beta'' \rightarrow \beta' \rightarrow \beta(+Si) \quad (1)$$

where SSSS is a super saturated solid solution [3–6]. The equilibrium phase  $\beta$  has empirical formula,  $Mg_2Si$ . The addition of Cu creates a new thermodynamically stable phase,  $Q$  [7,8]. Several additional metastable phases have been described in Cu containing alloys, including U1, U2, C,  $Q'$ ,  $\beta^1-2$ ,  $\beta^1-Cu$  and L [9–17].

These phases however do not appear in a linear sequence during ageing, rather they can co-exist, including within the same precipitate [14]. The metastable Cu containing phases sometimes occur as laths alongside rods, while rods are more common in Cu free alloys [7, 17]. The rods and laths both have their longest axis parallel to the matrix  $\langle 001 \rangle_{Al}$  lattice directions. Zandbergen et al. [18] observed in a 0.34 at.% Cu alloy that all the later stage precipitates contained Cu, including rods.

Some works have suggested that naturally aged solute clusters are thermally unstable and cannot transform into subsequent strengthening precipitates and that they are required to dissolve for the formation of

strengthening precipitates [5,19,20]. While others have suggested that solute clusters can be stable and transform into or nucleate further precipitates [4,21]. That only certain cluster chemistries and/or structures lead to further precipitation has also been suggested [6,21–26], with some solute clusters being stable, but which do not transform into or nucleate further precipitates. This range of suggested mechanisms in the literature, helps illustrate the complexity of the system.

Cu has been found to have a positive impact on reducing the negative effect of natural ageing in Al-6xxx [18,27]. As well as changing the phases present, this has been linked with a refinement in precipitate size and subsequent increase in precipitate number density [27,28]. Several works have seen that the rate at which an alloy hardens during natural ageing, which is due to the formation of solute clusters, is reduced by the addition of Cu [18,26,29,30]. In a previous work [31] we found that Cu did not influence the amount or rate of Mg and Si clustering during NA. In this work we will build upon that study to investigate the effect of subsequent ageing on the naturally aged samples.

The accurate and reliable quantification of solute clustering of Mg, Si and/or Cu in Al with atom probe tomography (APT) is a complex challenge, due the small nature of the features involved, that means the analysis is at the limitations of the spatial resolution achievable with atom probe [32]. User chosen parameters to select clusters can introduce significant bias into the results [33]. In this work we present

\* Corresponding author.

E-mail address: [james.famelton@brunel.ac.uk](mailto:james.famelton@brunel.ac.uk) (J.R. Famelton).

**Table 1**  
Compositions of Alloy H and Alloy L in at.%.

	Mg	Si	Cu	Al
Alloy L	0.6	0.6	0.1	bal.
Alloy H	0.6	0.6	0.3	bal.

a methodology which allows for consistent analysis of clusters and precipitates between datasets.

In this work, by directly observing solute clusters at different stages of the ageing process, we present insight into the mechanisms by which naturally aged solute clustering impacts the final mechanical properties of the alloy.

## 2. Experimental

Investigations were carried out on the same two alloys as in a previous work [31]. These are a low Cu (alloy L) and a high Cu (alloy H) variant of the same Al–Mg–Si–Cu alloy. The alloy compositions are given in Table 1.

The alloys were quenched from an above solvus heat treatment, then received a first period of natural ageing (NA1), were pre-aged at 170 °C for 30 min, received a second period of natural ageing (NA2) and were finally aged at 190 °C for 7 h. Samples referred to as immediate or i, spent less than 30 min at the first natural ageing step. While delayed, d, samples spent 8 weeks or more naturally ageing. Samples prepared after only natural ageing are referred to as NA, samples prepared after pre-ageing are referred to as PA and samples prepared after final ageing as FA. Differential scanning calorimetry (DSC) specimens were prepared in NA and PA conditions. APT specimens presented here were prepared in PA and FA conditions. APT specimens with only natural ageing, NA, were the subject of a previous work [31]. Samples are referred to by the alloy (H or L), NA1 duration (i or d) and ageing condition (NA, PA or FA) such that an alloy H sample, which has undergone more than 8 weeks of natural ageing before a pre-age treatment was carried out, is referred to as HdPA.

DSC experiments were carried out with a heating rate of 20 °C min<sup>-1</sup>, from 25 °C to 620 °C.

APT specimens were prepared using a two stage electropolishing method. Firstly, with a solution of 15% perchloric acid, 10% water and 75% acetic acid and an applied voltage of 20–10 V. This was followed by a solution of 1.2% perchloric acid, 0.8% water and 98% 2-butoxyethanol and an applied voltage of 10 V. APT datasets were obtained using a LEAP<sup>TM</sup> 5000 XR

APT data was reconstructed using the software, IVAS<sup>TM</sup>, with calibration of reconstruction parameters carried out using the methodology described by Gault et al. [34]. APT data was analysed using the commercial software; IVAS<sup>TM</sup> and APSuite<sup>TM</sup>; open source code packages, posgen and atomprobelab [35,36] and custom MATLAB scripts. Solute clusters and precipitates were extracted from the APT data using the maximum separation method. The choice of parameters used with this method are addressed in the relevant sections.

## 3. Results

### 3.1. Mechanical properties

The yield strengths of the four FA conditions are given in Table 2. The addition of more Cu in alloy H compared to alloy L, increases the strength in both i and d conditions. A short natural ageing period before pre-age, increases the strength in both alloys.

**Table 2**

$\sigma_y$ , yield strength of FA conditions. Ranges given are standard error,  $\sigma/\sqrt{n}$ , where  $\sigma$  is the standard deviation of measured yield strengths from  $n$  repeat tensile tests.

Condition	LdFA	LiFA	HdFA	HiFA
$\sigma_y$ (MPa)	276.8 ± 0.4	285.7 ± 0.3	306.6 ± 0.3	310.5 ± 0.9

### 3.2. DSC

DSC traces for alloy L and alloy H were measured and are shown in Figs. 1(a) and 1(b) respectively. For both alloys DSC traces were collected after natural ageing for a short and long period, and after subsequent pre-ageing. The two alloys behave similarly. The iNA samples are the only samples to show a peak at A, which is widely reported to be due to the formation of solute clusters [26,29,37,38]. It should be noted however these are not the same solute clusters as formed during extended natural ageing, as otherwise a dissolution peak B would be expected in the iNA trace which is not seen. Samples with extended natural ageing, dNA and dPA, all show an endothermic reaction at peak B, which is due to the dissolution of solute clusters formed during natural ageing [39]. This peak has been observed elsewhere when natural ageing has occurred [1,4,37,38,40–45].

The primary exothermic peak, C, is smaller in the iPA samples, which is likely due to the precipitates which have already formed during pre-ageing. This is not the case for delayed samples, with the dPA traces following very closely the dNA traces. Peak C may appear to occur at lower temperatures in the immediate samples, however this is likely due to the overlap between the endothermic and exothermic peaks B and C in the delayed samples, which makes the exothermic peak C appear to occur at a higher temperature.

### 3.3. APT before final ageing

Atom maps of representative areas of the 4 PA conditions are shown in Fig. 2. For brevity only Mg atoms are displayed. Si and Cu were also found in all solute clusters and precipitates, these elements are included in atom maps of the same areas in the supplementary material; figure A.1.

Two atom maps are shown for the HdPA condition. In these samples, several occurrences of groups of larger precipitates were found, as well as a matrix containing a high density of small solute clusters. These larger features are thought to have nucleated on dislocations. These rods occur in 3 orthogonal directions, thought to be the matrix  $\langle 001 \rangle_{Al}$  lattice directions. No precipitates on dislocations were observed in the LdPA condition. However, Poisson statistical analysis, gives a 95% confidence interval in the density of these combined dislocation precipitate features, of 0.3 to  $2 \times 10^3 \mu\text{m}^{-3}$  in HdPA and 0 to  $3 \times 10^3 \mu\text{m}^{-3}$  in LdPA. This shows that the rate of observation of these heterogeneous dislocation precipitates was not significantly high enough to conclude they occur at a higher rate in alloy H than in alloy L.

There is a clear visual difference between the iPA and dPA conditions (Figs. 2(a) and 2(d) compared to Figs. 2(b) and 2(e)), with both alloy's iPA conditions containing readily identifiable, relatively large, clusters of Mg atoms, while the dPA conditions do not contain these features. There is a further difference, between the LiPA and HiPA conditions; the larger features in LiPA, Fig. 2(d), have an elongated morphology, while the larger clusters in HiPA, Fig. 2(a), are spherical. The difference, if any, between the HdPA and LdPA conditions is less clear, and more quantified analysis of the solute clusters in the conditions is needed.

The solute clusters and precipitates were extracted from the APT data in order to more quantitatively compare size and number density. The maximum separation approach was used to cluster the data. This method has two user defined parameters,  $d_{max}$  and  $N_{min}$ , which are explained in detail elsewhere [46,47]. This method was chosen for its simplicity to implement and the simplicity to interpret the results.

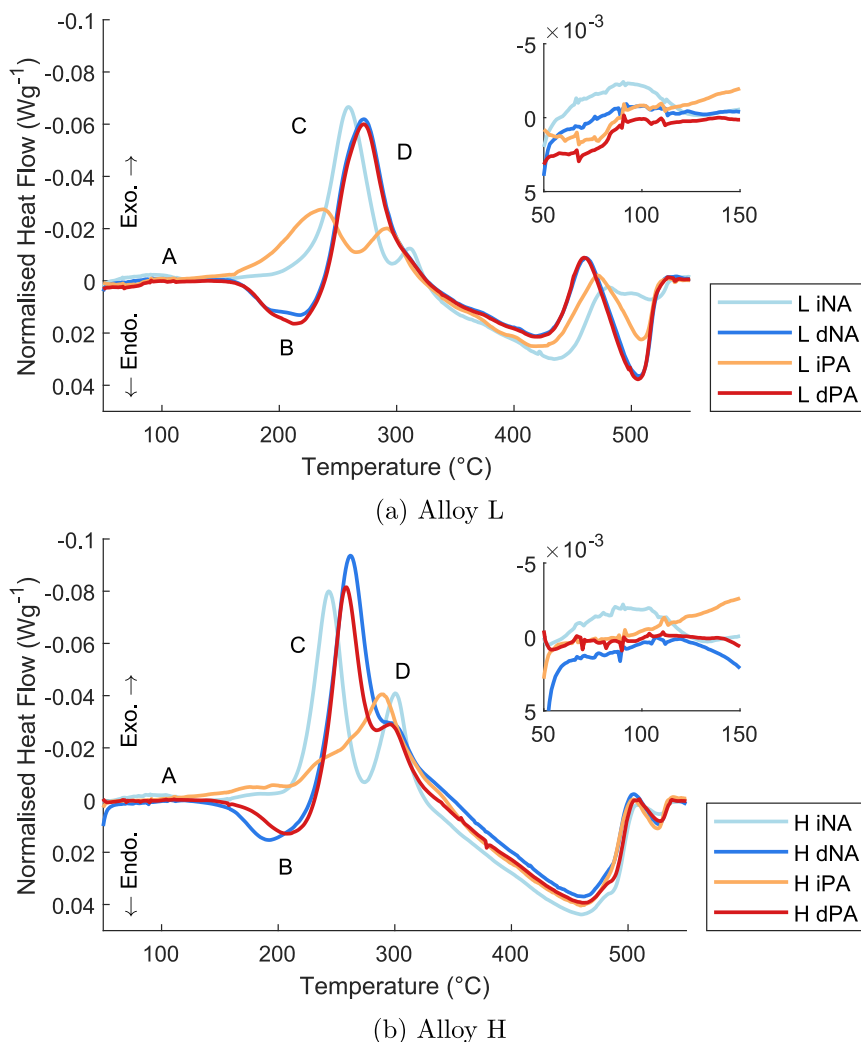


**Fig. 1.** DSC traces for alloy L and alloy H in naturally aged and pre-age conditions, with less than 30 min natural ageing (i) and over 8 weeks natural ageing (d). Endothermic dissolution peak, B, only occurs in the d samples which have undergone natural ageing.

Only Mg atoms were considered by the maximum separation algorithm in this instance. The value of the distance parameter was chosen as  $d_{max} = 0.53/\sqrt[3]{\rho_{Mg}}$ , where  $\rho_{Mg}$  is the density of Mg atoms in the reconstruction. The inclusion of the solute density term, corrects for any small variations in density and/or concentration between datasets, such that the same absolute value of  $d_{max}$  is applied to each dataset. The multiplying value, 0.53, was determined empirically to correspond to the normalised median 1st nearest neighbour distance between solute atoms in the investigated datasets, which had had their ionic identities shuffled (Figure A.3). This kind of random comparator dataset is also known as a relabelled dataset.

The result of using this value, is that the maximum separation algorithm selects from the APT data all the Mg atoms which are closer to another Mg atom than 50% of the Mg atoms in the relabelled dataset. The logic behind this choice is to maximise the number of true positives identified, ensuring all true positive clusters are selected from the dataset and appear as cohesive clusters, rather than a group of smaller clusters. All the regions with solute density greater than the average solute density are selected. By plotting the corresponding size distribution of solute clusters alongside the distribution expected in the relabelled dataset, one can observe how these extracted clusters, compare to the clusters expected in the relabelled dataset and determine which extracted clusters are likely to be false positives. Further details of this methodology and the determination of the empirical median 1st nearest neighbour distance are included in the supplementary material.

**Fig. 3** shows the distribution of clusters sizes, by plotting the number of Mg atoms detected in each cluster size bracket, normalised by the total number of Mg atoms detected. This normalisation is to account for differences in the size of APT datasets collected. In all the sub-figures the relabelled comparison data, RL, is included to show how many clusters and what cluster sizes are selected from the relabelled data using the median  $d_{max}$  value as described above. This RL dataset is the mean of a single relabel for each of the measured datasets. The individual relabels were seen to have low variation, as shown in the supplementary material; figure A.3.

As discussed qualitatively already, in the iPA conditions alloy H contains smaller clusters, which here are shown to contain 10–100 detected Mg atoms (**Fig. 3(a)**), while alloy L contains larger clusters, of 20–1000 detected Mg atoms (**Fig. 3(c)**). The two alloys have a similar overall number of Mg atoms selected as clustering, however in alloy H they are found in smaller and more numerous particles. Before the immediate pre-age is applied, it can be seen that both alloys have a similar size distribution of clusters, with very few features extracted which are above what is expected in a random solid solution. Alloy H contains more clusters in the range 10–20 atoms than alloy L.

In the dPA and dNA conditions, the majority of clusters extracted overlap in their size distribution with the clusters extracted from the relabelled dataset. However, there are significantly more clusters in the size range 5–20 Mg atoms, than is expected in the relabelled dataset. It can be seen in both alloy H and alloy L that there is little difference

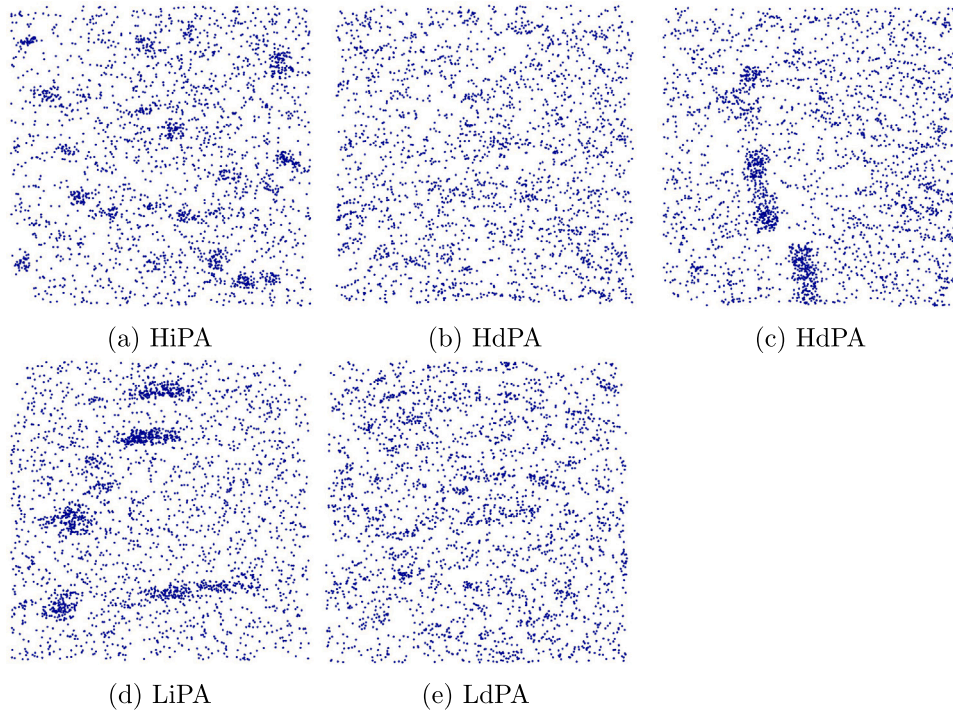


**Fig. 2.** Representative atom maps of the four pre-aged conditions. Each map is a  $50 \times 50 \times 5$  nm slice from the APT reconstruction. Only Mg atoms are shown for brevity, Si and Cu atom maps can be found in the supplementary material figure A.1. Two maps are shown for the HdPA condition, as heterogeneous nucleation on dislocations was observed in this condition, Fig. 2(c).

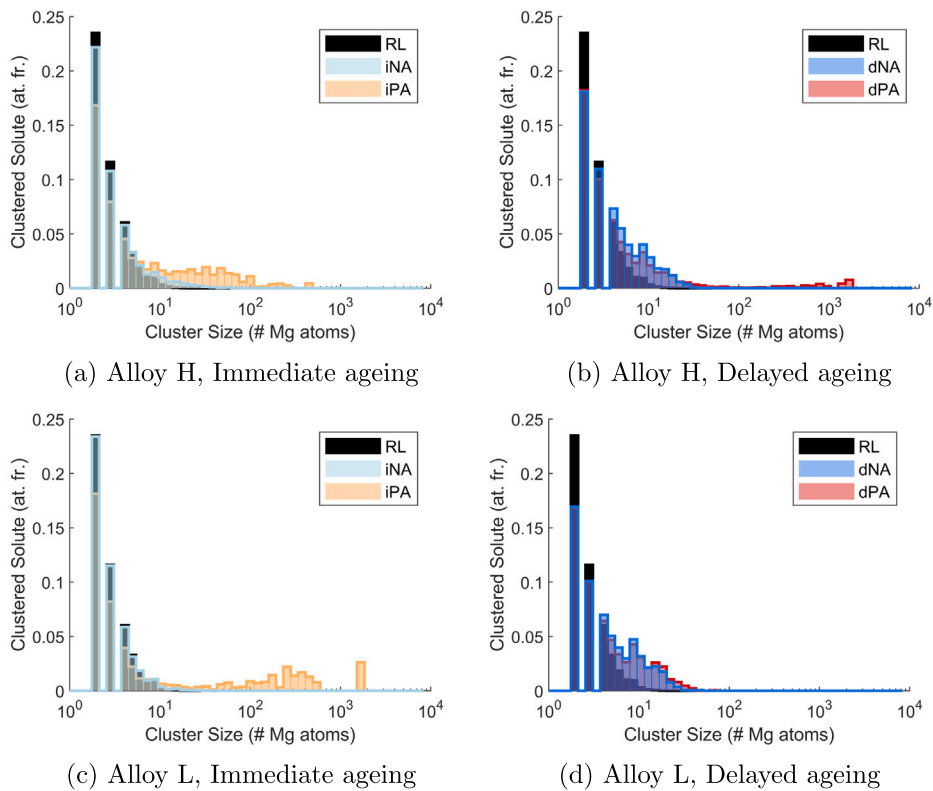


**Fig. 3.** Size distribution of clusters selected with maximum separation method,  $d_{max} = 0.53/\sqrt[3]{\rho_{Mg}}$ . Bar height is the fraction of total detected Mg atoms that were found clustered in that corresponding size range of cluster. In all plots the distribution of cluster sizes selected in a relabelled dataset at the same value of  $d_{max}$  are also shown.

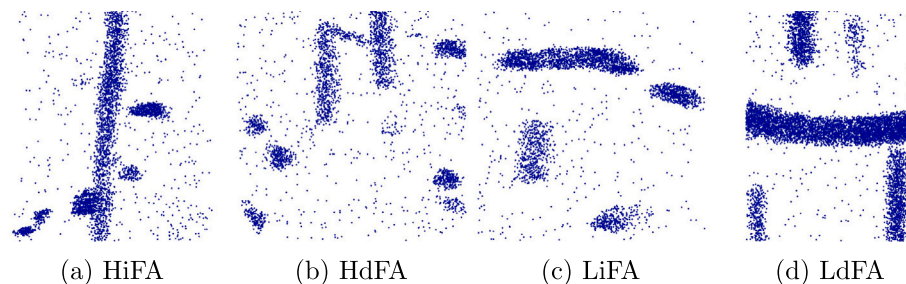


Fig. 4. Sections of atom maps of the four final aged conditions. Each map is a  $50 \times 50 \times 5$  nm slice from the APT reconstruction. Only Mg atoms are shown for brevity, Si and Cu atom maps can be found in the supplementary material figure A.2. All Mg atoms are shown, with no filtering from cluster identification applied.

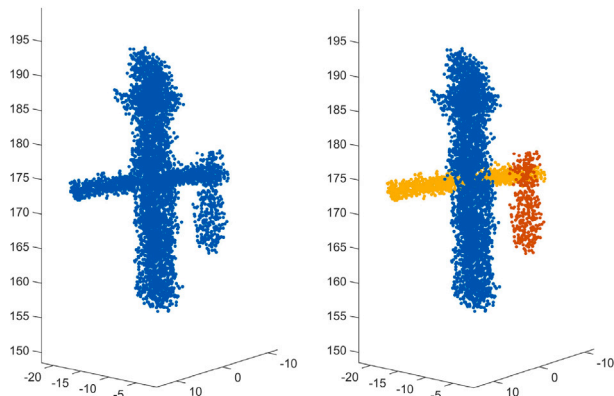


Fig. 5. An example of input and output of using a Gaussian Mixture Model to break up conjoined clusters. The user needs to supply the number of clusters to output.

between the size distribution and number density of these small clusters before and after pre-ageing. The density of clusters is also not seen to be significantly different between the two alloys. As mentioned already, some alloy H datasets contained a few larger particles, seen here in the size range 100–2000 Mg atoms; Fig. 3(b).

### 3.4. APT after final ageing

After final ageing all 4 conditions contain strengthening precipitates (Fig. 4). Precipitates were extracted using the same maximum separation methodology as described for the PA datasets. A minimum size cut-off of  $N_{min} = 21$  was applied to remove any potential false positive clusters. This correspond to the maximum size of cluster observed in the labelled datasets at this threshold of  $d_{max}$ ; Fig. 3. Some features, identified as a single feature with maximum separation, contained discrete convex regions; Fig. 5. This is not the result of using too great a value of  $d_{max}$ , but as can be seen in Fig. 5, is due to genuine overlap of precipitates. These discrete regions were separated using a Gaussian mixture model approach, as implemented in the statistics and machine learning toolbox in Matlab<sup>TM</sup>. The user is required to input how many regions to separate each feature into, with candidate features identified by having a high ratio of the features convex hull volume to  $\alpha$  hull volume ( $\alpha = 5d_{max}$  [48,49]). An example of the resulting precipitates after splitting is shown in Fig. 5.

Final precipitates extracted for all four FA conditions are shown in Fig. 6. Some precipitates were seen with an elongation in the secondary axis. These laths were observed in both alloy L and alloy H and often in linear features of parallel laths, thought to have nucleated along the same dislocation line (Fig. 6(a) and (c)).

Calculating the number density of these precipitates in APT data is complicated due to the high proportion of precipitates which are incident with the dataset edge. Methods such as used in [48], where edge incident precipitates are counted with half the weight of fully

captured precipitates work well for spherical features, but the assumptions used break down for the precipitates observed here, where this is a large range in precipitate size and aspect ratio. In order to best extract information about precipitate number density the authors have developed a methodology to measure the average spacing between precipitate centres. The methodology uses skeleton and watershed image processing algorithms on a binary voxel grid to form a skeleton for each precipitate (Fig. 7(b)), split the voxel grid into watershed domains (Fig. 7(c)) and measure the distance from domain surface to nearest skeleton segment (Fig. 7(d)).

Inter precipitate spacing,  $L$ , is a key metric in Orowan bowing of dislocations around precipitates, with the expected increase in shear stress due to bowing;  $\tau_o = Gb/L$ , where  $G$  is the shear modulus and  $b$  the magnitude of the burgers vector. The precipitate spacing used in the derivation of shear stress due to bowing, is precipitate edge-to-edge, i.e. the smallest gap the dislocation must pass through, whereas here we measured centre-to-centre. As an approximation we believe this will have little impact on the measured trend, as precipitate size is small compared to the spacing and the different conditions have approximately similar precipitate widths. Attempting to identify the precipitate edge-to-edge distance in APT would likely introduce more uncertainty, due the local magnification of precipitates in Al-6xxx as measured by APT [50].

This methodology to measure average inter precipitate spacing was applied to datasets in the FA condition. Fig. 8 shows the inverse precipitate spacing against yield strength for each of the 4 conditions. A linear trend can be observed, as is expected for Orowan bowing of dislocations. It is clear that the Cu addition to the alloy has increased precipitate number density, reducing inter precipitate spacing and hence increasing yield strength, in agreement with other literature results [28]. In the high Cu alloy the amount of additional strength in the immediately aged material is explained by a higher density of precipitates. In the low Cu alloy L, the immediate aged material is also stronger, however the precipitates are not measurably closer together. The LdFA condition had the smallest amount of APT data collected across the 4 conditions and correspondingly there is the greatest uncertainty in this measurement. Total analysed volumes for HdFA, HiFA, LdFA and LiFA were  $1.2 \times 10^6$ ,  $5.9 \times 10^5$ ,  $3.1 \times 10^5$  and  $7.8 \times 10^5$  nm<sup>3</sup> respectively. Smaller individual dataset volumes may also be biasing the result, as relatively large inter precipitate spacings cannot be measured in a small dataset. Further results are needed to confirm that the difference in strength between LiFA and LdFA is due to precipitate number density, although this mechanism has been observed elsewhere [24].

## 4. Discussion

Insight into the mechanism by which Cu addition and immediate ageing act to increase precipitate number density can be gained by looking at the smallest precipitates present after FA.

While overall precipitate number density is hard to measure, due to precipitates captured at the edge of the field-of-view, some precipitates,

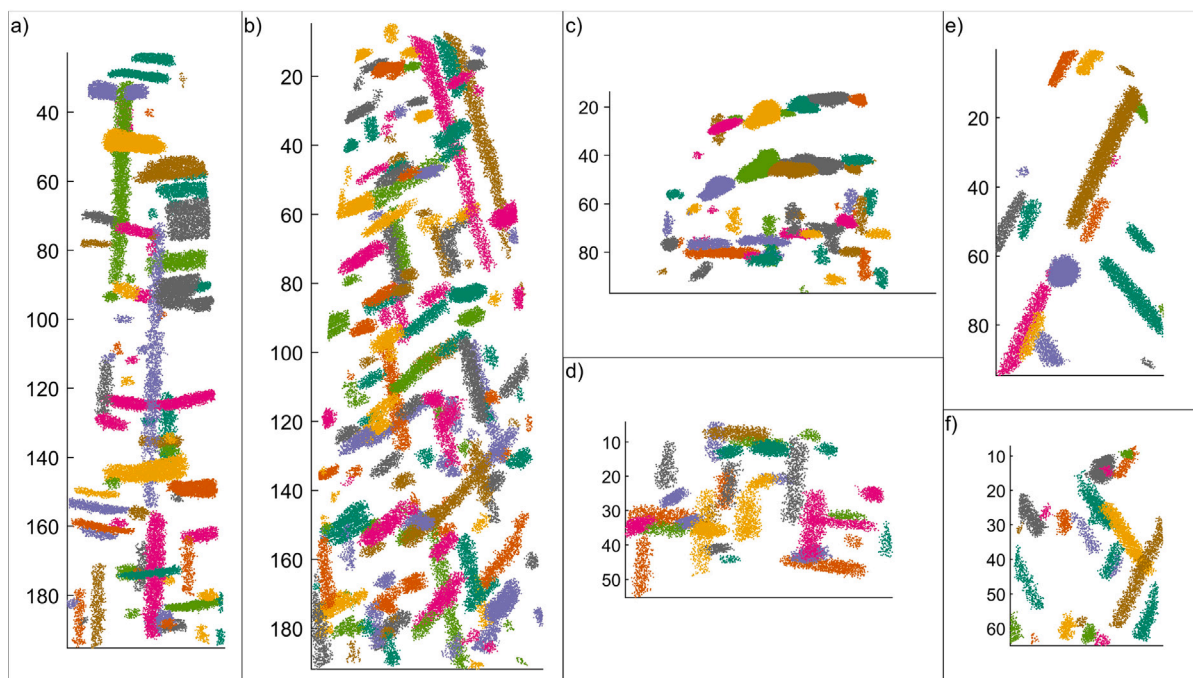


Fig. 6. Selected atom maps of precipitates identified from FA datasets with the maximum separation algorithm. Only Mg atoms are shown, with separately identified precipitates highlighted with different colours. (a) HiFA, (b) HdPA, (c) and (d) LiFA, (e) and (f) LdFA. (For interpretation of the references to colour in this figure legend, the reader is referred to the web version of this article.)

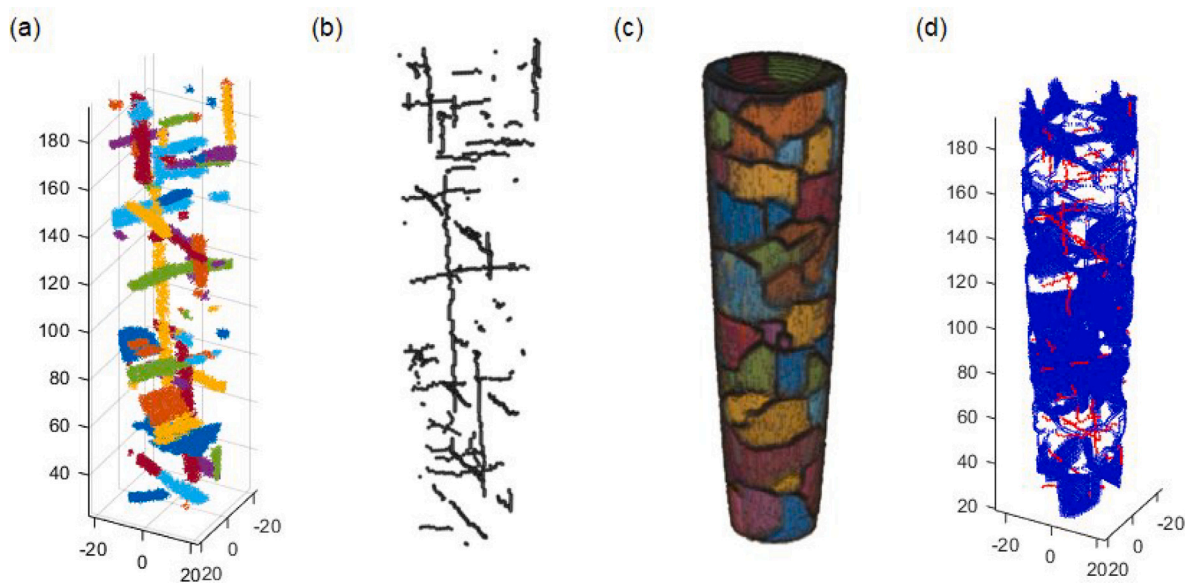


Fig. 7. (a) Precipitates extracted using maximum separation method. These are used to form a binary voxel grid. (b) voxel skeleton of each precipitate (c) domains formed from watershed of binary voxel grid. (d) surface of each domain in blue and skeleton in red. Mean distance from points on the domain surface to the nearest skeleton segment is computed. The voxels used were cubes, with side length =  $d_{max}$  and no de-localisation was applied. (For interpretation of the references to colour in this figure legend, the reader is referred to the web version of this article.)

in particular the smallest, can be observed which have been fully captured. The number density of precipitates between size 21–100 detected Mg atoms in the 4 FA conditions are shown in Fig. 9. All Mg atoms in the selected features were required to be 2 nm from the dataset surface to avoid detecting the edges of larger precipitates. 100 Mg atoms was chosen as a semi-arbitrary cut-off for the maximum size of these smallest precipitates, but it is noted that this size range corresponds roughly with the clusters identified in HiPA, HdPA and LdPA in Fig. 3. The LiPA features were larger on average.

The density of these small feature corresponds to the overall spacing of the precipitates and the yield strength in Fig. 8. Several features

were identified in 3 of the 4 conditions (not in LdPA), where a large precipitate was found adjacent to a small precipitate. Examples of these features are shown in Fig. 10. The authors believe these small precipitates are features which were present in the alloy after pre-ageing and have acted as nucleation sites for further larger precipitates. It would otherwise be unexpected for these features to have this morphology, which has a larger surface area rather than forming a single rod.

In Fig. 10(b), three regions were selected from the clustering Mg, as it was noted there is a change in the density of Mg and the width of rod partway along the rod; boundary between orange and green, cluster 2 and cluster 3 regions. This could be due a change in phase

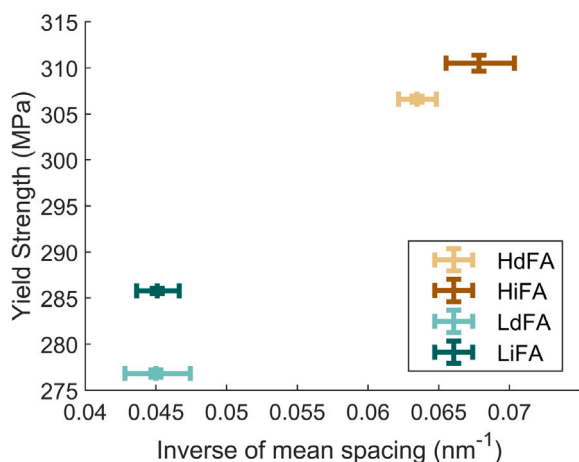


**Fig. 8.** Sample tensile yield strength plotted against the inverse of the mean precipitate spacing. Error bars in yield strength are standard error across multiple tensile tests. Error bars in the inverse spacing is the standard error based on the number of precipitates measured,  $n_{ppi}$ .  $stder. = \sigma / \sqrt{n_{ppi}}$ , where  $\sigma$  is the standard deviation of all domain surface to voxel skeleton distances measured, which is significantly more measurements than  $n_{ppi}$ , but these are not independent measurements.

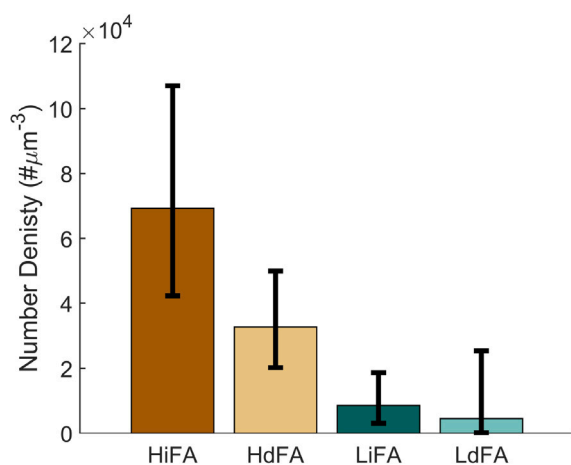


**Fig. 9.** Number density of precipitates between 21 and 100 detected Mg atoms in size. This is only precipitates which were fully encapsulated in the field of view and which were a minimum of 2 nm from dataset edge.

and nucleation of a separate precipitate between the regions, cluster 2 and cluster 3. This was the only such feature observed.

Not all rod precipitates were observed with these small precipitates at one end or part way along the rod. It is probable that if rods have nucleated on small precipitates that in many cases these have then been incorporated into the larger feature. The sites shown in Fig. 10 are in the two alloy H conditions, however such sites were also observed in LiFA (figure A.4). The lack of nucleation sites in LdFA is most likely linked to the lower volume of material sampled and the low density of small precipitates (Fig. 9) and such sites could be observed if more volume was sampled.

The authors propose the following mechanism to explain these observations. The role of Cu in the immediately aged samples is to modify the size and number density of nuclei formed during pre-ageing. Cu increases the number density of nuclei. We propose that this is due to a reduction in the precipitate-to-matrix interfacial energy, which would explain the change in precipitate morphology with the addition of more Cu. This reduction in interfacial energy may be due to changes in the precipitate's phase and internal structure or due to Cu changing the structure of the precipitate-to-matrix interface. The high Cu alloy

pre-aged precipitates are spherical and show no preferential growth direction. This high density of nuclei then remain stable at the final ageing temperature, as observed via the absence of a dissolution peak B in DSC traces, and this leads to an overall higher number density of precipitates in HiFA than LiFA.

In the delayed ageing samples, where clusters have formed during natural ageing, Cu is not seen to have changed the characteristics of these cluster after pre-ageing. A similar fraction of solute is clustered in LdPA and HdPA and the clusters are similarly sized. In both alloys a dissolution peak B is seen to begin when these alloys are raised to the final ageing temperature. Where the Cu creates a difference is in the number of small precipitates present in the material after FA. The authors propose that Cu is stabilising more clusters, so they do not dissolve in the initial stages of FA. These surviving clusters and/or small precipitates can then act as nucleation sites for further precipitates, leading to an overall higher number density of precipitates in HdFA than LdFA.

## 5. Conclusions

Immediate pre-ageing of both high and low Cu alloy variants produces stable nuclei, which leads to a high final density of precipitates. The high Cu addition alloy has a higher number density of nuclei after pre-ageing, due to a modification in size and morphology, and thus a subsequent higher number density of final precipitates and correspondingly, yield strength.

Pre-ageing after significant natural ageing, does not create stable nuclei, instead a population of largely unstable solute clusters are present in both alloys. Cu is seen to increase the density of small precipitates present after FA and is thought to be increasing the stability of more solute clusters so a smaller fraction dissolve. This leaves a higher density of nucleation sites and thus a higher overall precipitate number density and strength in the high Cu alloy variant, compared to the low Cu variant.

## CRediT authorship contribution statement

**J.R. Famelton:** Writing – review & editing, Writing – original draft, Visualization, Software, Investigation, Formal analysis, Conceptualization. **C.A. Williams:** Supervision, Resources. **C. Barbatti:** Supervision, Resources, Funding acquisition. **P.A.J. Bagot:** Supervision. **M.P. Moody:** Writing – review & editing, Supervision, Funding acquisition.

## Declaration of competing interest

The authors declare that they have no known competing financial interests or personal relationships that could have appeared to influence the work reported in this paper.

## Acknowledgements

The authors would like to thank Constellium for providing the materials and financially supporting this research alongside the Engineering and Physical Science Research Council (EPSRC) through studentship 1922133. The authors would also like to thank Constellium staff for their support of the DSC experiments. The authors are grateful to EPSRC for funding of the LEAP 5000XR for the UK National Atom Probe Facility through grant EP/M022803/1.

## Appendix A. Supplementary data

Supplementary material related to this article can be found online at <https://doi.org/10.1016/j.mtla.2025.102448>.

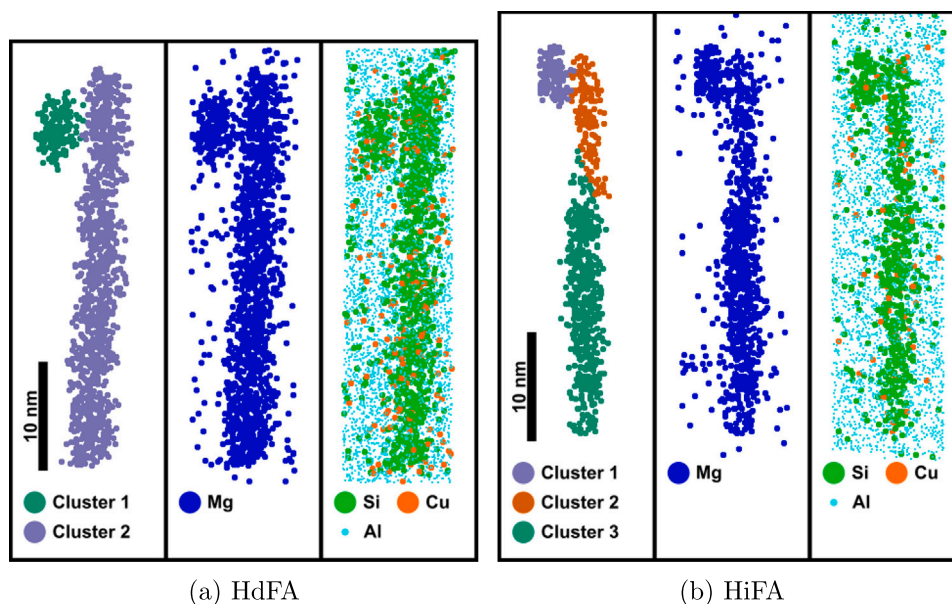


**Fig. 10.** Atom maps of potential nucleation sites observed in alloy H. Three panels are shown for each site. Left: Mg atoms extracted by maximum separation method, coloured by clusters split by Gaussian mixture method (Fig. 5). Central: All Mg atom before maximum separation applied. Right: All Si and Cu and 5% of Al in the same region. The atom maps in (a) and (b) have depths 8 nm and 6 nm respectively. Such sites were also observed in alloy L, figure A.4. (For interpretation of the references to colour in this figure legend, the reader is referred to the web version of this article.)

## Data availability

The raw and processed data required to reproduce these findings is confidential.

## References

- [1] P. Dumitraschewitz, S.S.A. Gerstl, L.T. Stephenson, P.J. Uggowitzer, S. Pogatscher, Clustering in Age-Hardenable Aluminum Alloys, *Adv. Eng. Mater.* 20 (10) (2018) 1800255, <http://dx.doi.org/10.1002/adem.201800255>.
- [2] D.W. Pashley, J. Rhodes, A. Sendorek, Delayed Ageing in Aluminium-Magnesium-Silicon Alloys - Effect on structure and Mechanical Properties, *J. Inst. Met.* 94 (2) (1966) 41.
- [3] J. Banhart, C.S.T. Chang, Z. Liang, N. Wanderka, M.D.H. Lay, A.J. Hill, Natural Aging in Al-Mg-Si Alloys - A Process of Unexpected Complexity, *Adv. Eng. Mater.* 12 (7) (2010) 559–571, <http://dx.doi.org/10.1002/adem.201000041>.
- [4] G.H. Tao, C.H. Liu, J.H. Chen, Y.X. Lai, P.P. Ma, L.M. Liu, The influence of Mg to Si ratio on the negative natural aging effect in Al-Mg-Si-Cu alloys, *Mater. Sci. Eng. A* 642 (2015) 241–248, <http://dx.doi.org/10.1016/j.msea.2015.06.090>.
- [5] A. Poznak, R.K. Marceau, P. Sanders, Composition dependent thermal stability and evolution of solute clusters in Al-Mg-Si analyzed using atom probe tomography, *Mater. Sci. Eng.: A* 721 (2018) 47–60, <http://dx.doi.org/10.1016/j.msea.2018.02.074>.
- [6] S. Pogatscher, H. Antrekowitsch, H. Leitner, T. Ebner, P. Uggowitzer, Mechanisms controlling the artificial aging of Al-Mg-Si Alloys, *Acta Mater.* 59 (9) (2011) 3352–3363, <http://dx.doi.org/10.1016/j.actamat.2011.02.010>.
- [7] D. Chakrabarti, D.E. Laughlin, Phase relations and precipitation in Al-Mg-Si alloys with Cu additions, *Prog. Mater. Sci.* 49 (3–4) (2004) 389–410, [http://dx.doi.org/10.1016/S0079-6425\(03\)00031-8](http://dx.doi.org/10.1016/S0079-6425(03)00031-8).
- [8] R.K. Marceau, A. de Vaucorbeil, G. Sha, S. Ringer, W. Poole, Analysis of strengthening in AA6111 during the early stages of aging: Atom probe tomography and yield stress modelling, *Acta Mater.* 61 (2013) 7285–7303, <http://dx.doi.org/10.1016/j.actamat.2013.08.033>.
- [9] S.J. Andersen, C.D. Marioara, A. Frøseth, R. Vissers, H.W. Zandbergen, Crystal structure of the orthorhombic U2-Al4Mg4Si4 precipitate in the Al-Mg-Si alloy system and its relation to the  $\beta'$  and  $\beta''$  phases, *Mater. Sci. Eng.: A* 390 (1–2) (2005) 127–138, <http://dx.doi.org/10.1016/J.MSEA.2004.09.019>.
- [10] S.J. Andersen, C.D. Marioara, R. Vissers, A. Frøseth, H.W. Zandbergen, The structural relation between precipitates in Al-Mg-Si alloys, the Al-matrix and diamond silicon, with emphasis on the trigonal phase U1-MgAl2Si2, *Mater. Sci. Eng. A* 444 (1–2) (2007) 157–169, <http://dx.doi.org/10.1016/J.MSEA.2006.08.084>.
- [11] M. Torsæter, F.J.H. Ehlers, C.D. Marioara, S.J. Andersen, R. Holmestad, Applying precipitate-host lattice coherency for compositional determination of precipitates in Al-Mg-Si-Cu alloys, *Phil. Mag.* 92 (31) (2012) 3833–3856, <http://dx.doi.org/10.1080/14786435.2012.693214>.
- [12] L. Arnberg, B. Aurivillius, E. Wahlström, G. Malmros, J. Sjöblom, T.G. Strand, V.F. Sukhoverkhov, The Crystal Structure of Al(x)Cu2Mg(12-x)Si7, (h-AlCuMgSi), *Acta Chem. Scand.* 34a (1980) 1–5, <http://dx.doi.org/10.3891/acta.chem.scand.34a-0001>.
- [13] C. Wolverton, Crystal structure and stability of complex precipitate phases in Al-Cu-Mg-(Si) and Al-Zn-Mg alloys, *Acta Mater.* 49 (16) (2001) 3129–3142, [http://dx.doi.org/10.1016/S1359-6454\(01\)00229-4](http://dx.doi.org/10.1016/S1359-6454(01)00229-4).
- [14] J. Sunde, C.D. Marioara, A. van Helvoort, R. Holmestad, The evolution of precipitate crystal structures in an Al-Mg-Si-(Cu) alloy studied by a combined HAADF-STEM and SPED approach, *Mater. Charact.* 142 (2018) 458–469, <http://dx.doi.org/10.1016/j.matchar.2018.05.031>.
- [15] C.D. Marioara, J. Nakamura, K. Matsuda, S.J. Andersen, R. Holmestad, T. Sato, T. Kawabata, S. Ikeno, HAADF-STEM study of  $\beta'$ -type precipitates in an over-aged Al-Mg-Si-Ag alloy, *Phil. Mag.* 92 (9) (2012) 1149–1158, <http://dx.doi.org/10.1080/14786435.2011.642319>.
- [16] J.K. Sunde, O. Paulsen, S. Wenner, R. Holmestad, Precipitate statistics in Al-Mg-Si-Cu alloy from scanning precession electron diffraction data, *J. Phys.: Conf. Ser.* 902 (2017) 12022, <http://dx.doi.org/10.1088/1742-6596/902/1/012022>.
- [17] C.D. Marioara, S.J. Andersen, T.N. Stene, H. Hasting, J. Walmsley, A.T.J. Van Helvoort, R. Holmestad, The effect of Cu on precipitation in Al-Mg-Si alloys, *Phil. Mag.* 87 (23) (2007) 3385–3413, <http://dx.doi.org/10.1080/14786430701287377>.
- [18] M. Zandbergen, A. Cerezo, G. Smith, Study of precipitation in Al-Mg-Si Alloys by atom probe tomography II. Influence of Cu additions, *Acta Mater.* 101 (2015) 149–158, <http://dx.doi.org/10.1016/j.actamat.2015.08.018>.
- [19] S. Esmaili, X. Wang, D.J. Lloyd, W.J. Poole, On the Precipitation-Hardening Behavior of the Al-Mg-Si-Cu Alloy AA6111, *Met. Mater. Trans. A* 34 (13) (2003) 751–763.
- [20] M. Murayama, K. Hono, Pre-precipitate clusters and precipitation processes in Al-Mg-Si alloys, *Acta Mater.* 47 (5) (1999) 1537–1548, [http://dx.doi.org/10.1016/S1359-6454\(99\)00033-6](http://dx.doi.org/10.1016/S1359-6454(99)00033-6).
- [21] C.D. Marioara, S.J. Andersen, C. Hell, J. Frafjord, J. Friis, R. Bjørge, I.G. Ringdalen, O. Engler, R. Holmestad, Atomic structure of clusters and GP-zones in an Al-Mg-Si alloy, *Acta Mater.* 269 (2024) 119811, <http://dx.doi.org/10.1016/J.ACTAMAT.2024.119811>.
- [22] A. Serizawa, S. Hirotsawa, T. Sato, Three-Dimensional Atom Probe Characterization of Nanoclusters Responsible for Multistep Aging Behavior of an Al-Mg-Si Alloy, *Met. Mater. Trans. A* 39 (2) (2008) 243–251, <http://dx.doi.org/10.1007/s11661-007-9438-5>.
- [23] Z. Cui, H. Jiang, D. Zhang, L. Rong, Inhibiting of the negative natural aging effect in Al-Mg-Si alloys, *Mater. Sci. Eng.: A* 894 (2024) 146196, <http://dx.doi.org/10.1016/J.MSEA.2024.146196>.
- [24] M. Torsæter, H.S. Hasting, W. Lefebvre, C.D. Marioara, J.C. Walmsley, S.J. Andersen, R. Holmestad, The influence of composition and natural aging on clustering during preaging in Al-Mg-Si alloys, *J. Appl. Phys.* 108 (7) (2010) 073527, <http://dx.doi.org/10.1063/1.3481090>.

- [25] M. Zandbergen, Q. Xu, A. Cerezo, G. Smith, Study of precipitation in Al–Mg–Si alloys by Atom Probe Tomography I. Microstructural changes as a function of ageing temperature, *Acta Mater.* 101 (2015) 136–148, <http://dx.doi.org/10.1016/j.actamat.2015.08.017>.
- [26] M. Werinos, H. Antrekowitsch, T. Ebner, R. Prillhofer, P. Uggowitzer, S. Pogatscher, Hardening of Al–Mg–Si alloys: Effect of trace elements and prolonged natural aging, *Mater. Des.* 107 (2016) 257–268, <http://dx.doi.org/10.1016/j.matdes.2016.06.014>.
- [27] S. Wenner, C.D. Marioara, S.J. Andersen, R. Holmestad, Effect of room temperature storage time on precipitation in Al–Mg–Si(Cu) alloys with different Mg/Si ratios, *Int. J. Mater. Res.* 103 (8) (2012) 948–954, <http://dx.doi.org/10.3139/146.110795>.
- [28] P. Aster, P. Dumitraschkewitz, P.J. Uggowitzer, M.A. Tunes, F. Schmid, L. Stemper, S. Pogatscher, Unraveling the potential of Cu addition and cluster hardening in Al–Mg–Si alloys, *Materialia* 36 (2024) 102188, <http://dx.doi.org/10.1016/j.mtla.2024.102188>.
- [29] J. Kim, E. Kobayashi, T. Sato, Influence of natural aging time on two-step aging behavior of Al–Mg–Si(Cu) alloys, *Mater. Trans.* 56 (11) (2015) 1771–1780, <http://dx.doi.org/10.2320/matertrans.L-M2015824>.
- [30] Z. Jia, L. Ding, L. Cao, R. Sanders, S. Li, Q. Liu, The Influence of Composition on the Clustering and Precipitation Behavior of Al–Mg–Si–Cu Alloys, *Met. Mater. Trans. A* 48A (2017) 459–473, <http://dx.doi.org/10.1007/s11661-016-3850-7>.
- [31] J. Famelton, C. Williams, C. Barbatti, P. Bagot, M. Moody, Point excess solute: A new metric for quantifying solute segregation in atom probe tomography datasets including application to naturally aged solute clusters in Al–Mg–Si(Cu) alloys, *Mater. Charact.* 206 (2023) 113402, <http://dx.doi.org/10.1016/j.matchar.2023.113402>.
- [32] F. De Geuser, B. Gault, Metrology of small particles and solute clusters by atom probe tomography, *Acta Mater.* 188 (15) (2020) 406–415, <http://dx.doi.org/10.1016/j.actamat.2020.02.023>, [arXiv:1910.10532](https://arxiv.org/abs/1910.10532).
- [33] E.A. Marquis, V. Araullo-Peters, Y. Dong, A. Etienne, S. Fedotova, K. Fujii, K. Fukuya, E. Kuleshova, A. Lopez, A. London, S. Lozano-Perez, Y. Nagai, K. Nishida, B. Radiguet, D. Schreiber, N. Soneda, M. Thuvander, T. Toyama, F. Sefta, P. Chou, On the Use of Density-Based Algorithms for the Analysis of Solute Clustering in Atom Probe Tomography Data, in: J. J., P. D., W. M. (Eds.), *Proceedings of the 18th International Conference on Environmental Degradation of Materials in Nuclear Power Systems - Water Reactors*, Springer US, 2019, pp. 2097–2113, [http://dx.doi.org/10.1007/978-3-030-04639-2\\_141](http://dx.doi.org/10.1007/978-3-030-04639-2_141).
- [34] B. Gault, M.P. Moody, F. De Geuser, G. Tsafnat, A. La Fontaine, L.T. Stephenson, D. Haley, S.P. Ringer, Advances in the calibration of atom probe tomographic reconstruction, *J. Appl. Phys.* 105 (3) (2009) 034913, <http://dx.doi.org/10.1063/1.3068197>.
- [35] D. Haley, Posgen 0.0.4, 2020, <https://apptools.sourceforge.io/> (Accessed 30 June 2020).
- [36] A.J. London, *Atomprobelab v2.2*, 2020.
- [37] A.K. Gupta, D.J. Lloyd, Study of precipitation kinetics in a super purity Al-0.8 % Mg-0.9 % Si alloy using differential scanning calorimetry, *Met. Mater. Trans. A* 30 (13) (1999) 879–890, <http://dx.doi.org/10.1007/s11661-999-1021-9>.
- [38] Z. Yang, J. Banhart, Natural and artificial ageing in aluminium alloys – the role of excess vacancies, *Acta Mater.* 215 (2021) 117014, <http://dx.doi.org/10.1016/j.actamat.2021.117014>.
- [39] Z. Yang, I. Erdle, C. Liu, J. Banhart, Clustering and precipitation in Al–Mg–Si alloys during linear heating, *J. Mater. Sci. Technol.* 120 (2022) 78–88, <http://dx.doi.org/10.1016/J.JMST.2021.11.062>.
- [40] P. Dumitraschkewitz, P.J. Uggowitzer, S.S. Gerstl, J.F. Löffler, S. Pogatscher, Size-dependent diffusion controls natural aging in aluminium alloys, *Nat. Commun.* 10 (1) (2019) 1–6, <http://dx.doi.org/10.1038/s41467-019-12762-w>.
- [41] Y. Ohmori, L.C. Doan, Y. Matsuura, S. Kobayashi, K. Nakai, Morphology and crystallography of  $\beta$ -Mg<sub>2</sub>Si precipitation in Al–Mg–Si alloys, *Mater. Trans.* 42 (12) (2001) 2576–2583.
- [42] M. Takeda, F. Ohkubo, T. Shirai, K. Fukui, Stability of metastable phases and microstructures in the ageing process of Al–Mg–Si ternary alloys, *J. Mater. Sci.* 33 (9) (1998) 2385–2390.
- [43] I. Dutta, S.M. Allen, A calorimetric study of precipitation in commercial aluminium alloy 6061, *J. Mater. Sci. Lett.* 10: 6 10 (6) (1991) 323–326, <http://dx.doi.org/10.1007/BF00719697>.
- [44] A.K. Gupta, D. Lloyd, S. Court, Precipitation hardening in Al–Mg–Si alloys with and without excess Si, *Mater. Sci. Eng.: A* 316 (1–2) (2001) 11–17, [http://dx.doi.org/10.1016/S0921-5093\(01\)01247-3](http://dx.doi.org/10.1016/S0921-5093(01)01247-3).
- [45] A.K. Gupta, D. Lloyd, *The Precipitation in a Super Purity Al–Mg–Si alloy*, in: *The 3rd International Conference on Aluminium Alloys*, Vol. 2, 1992, pp. 21–25, June.
- [46] J.M. Hyde, C.A. English, *An Analysis of the Structure of Irradiation induced Cu-enriched Clusters in Low and High Nickel Welds*, in: *MRS Proceedings*, Vol. 650, Cambridge University Press, 2000, p. R6.6, <http://dx.doi.org/10.1557/PROC-650-R6.6>.
- [47] L.T. Stephenson, M.P. Moody, P.V. Liddicoat, S.P. Ringer, New Techniques for the Analysis of Fine-Scaled Clustering Phenomena within Atom Probe Tomography (APT) Data, *Microsc. Microanal.* 13 (06) (2007) 448–463, <http://dx.doi.org/10.1017/S1431927607070900>.
- [48] B.M. Jenkins, A.J. London, N. Riddle, J.M. Hyde, P.A. Bagot, M.P. Moody, Using alpha hulls to automatically and reproducibly detect edge clusters in atom probe tomography datasets, *Mater. Charact.* 160 (2020) 110078, <http://dx.doi.org/10.1016/j.matchar.2019.110078>.
- [49] P. Felfer, A. Ceguerra, S. Ringer, J. Cairney, Applying computational geometry techniques for advanced feature analysis in atom probe data, *Ultramicroscopy* 132 (2013) 100–106, <http://dx.doi.org/10.1016/J.ULTRAMIC.2013.03.004>.
- [50] F. Vurpillot, A. Bostel, D. Blavette, Trajectory overlaps and local magnification in three-dimensional atom probe, *Appl. Phys. Lett.* 76 (21) (2000) 3127–3129, <http://dx.doi.org/10.1063/1.126545>.